Point spread function of the polarized light field microscope

Mai Thi Tran[1,*] AND Rudolf Oldenbourg[2,3]

[1]*VinUniversity, Hanoi, Vietnam*
[2]*Marine Biological Laboratory, Woods Hole, Massachusetts 02543, USA*
[3]*e-mail: rudolfo@mbl.edu*
Corresponding author: mai.tt@vinuni.edu.vn

We examined the point spread function of the polarized light field microscope and established a computational framework to solve the forward problem in polarized light field imaging, for the purpose of furthering its use as a quantitative tool for measuring three-dimensional maps of the birefringence of transparent objects. We recorded experimental polarized light field images of small calcite crystals and of larger birefringent objects and compared our experimental results to numerical simulations based on polarized light ray tracing. We find good agreement between all our experiments and simulations, which leads us to propose polarized light ray tracing as one solution to the forward problem for the complex, nonlinear imaging mode of the polarized light field microscope. Solutions to the ill-posed inverse problem might be found in analytical methods and/or deep learning approaches that are based on training data generated by the forward solution presented here.   © 2022 Optica Publishing Group under the terms of the Optica Open Access Publishing Agreement

1. INTRODUCTION

In microscopy, the experimental point spread function is represented by a series of images of a small point source as it moves in and out of focus. The in-focus image represents the tightest intensity spot the microscope optics can generate of a point source, while the out-of-focus images represent the intensity distribution that becomes more and more blurred the further the point emitter is moved out of focus. The point spread function is a sensitive indicator of the resolution and imaging properties of a microscope lens system [1,2].

The point spread function of the polarized light microscope is a function not only of the position of an anisotropic point object but also of the orientation of its polarizability tensor. In a previous study using the LC-PolScope for recording polarized light images of small calcite crystals, we illustrated the relationship between the observed in- and out-of-focus images and the orientation of the optic axis of the subresolution crystals [3]. The study also highlighted the need for combining observations not only of different positions of the crystals but also along different viewing directions to establish the complete point spread function.

With this need in mind, we developed the scanned-aperture LC-PolScope, which introduced a configurable mask in the aperture plane of the condenser optics of an otherwise unchanged LC-PolScope setup [4]. Using this setup, we recorded PolScope images of a weakly birefringent, spherically symmetric biological object called aster, that features dense arrays of a biopolymer (microtubules) that radiate out from a common center. By employing five different configurations of the aperture mask, we recorded PolScope aster images that each was produced with a different tilt angle of the chief ray of the illumination cone with respect to the microscope axis. We also developed reconstruction algorithms that combined the images obtained along different illumination directions to reveal the local 3D optic axis orientation in this biological Koosh ball.

A similar experimental approach with a configurable mask in the illumination optics, and brand-new algorithms for reconstructing the 3D permittivity tensor of thick phase objects, including birefringent specimens, was recently implemented by the Group of Shalin Mehta at the CZI Biohub [5].

A somewhat different approach to generating images along different viewing directions became possible by the introduction of the light field microscope by Marc Levoy at Stanford University [6]. Instead of using a configurable aperture mask, the light field camera includes an array of microlenses that project small conoscopic views of the object scene onto the camera sensor. The only change necessary to convert a regular light microscope into a light field microscope is exchanging the regular camera with a light field camera that is a combination of a microlens array and a 2D light sensor. The microlens array is placed in the intermediate image plane of the microscope, followed by the sensor in the focal plane of the microlenses. Hence, the light sensor captures an array of images of the objective lens's back aperture, each one specific to the

location of the microlens in the image plane. In microscopy, the image of the back focal plane of the objective lens is called the conoscopic image, while the image in the intermediate image plane of the microscope is called the orthoscopic image. A light field image is a combination of both, i.e., conoscopic images on a regular grid sampling the image/object plane.

Intrigued by the possibility of combining orthoscopic and conoscopic views, two imaging modes well established in traditional polarized light microscopy, we explored the use of a light field camera in an LC-PolScope setup, creating the light field LC-PolScope [7]. As a first application, we analyzed a thin, polycrystalline calcite film and were able to determine the azimuth and inclination angle of the optic axis orientation of each crystalline region in the sample, all at once, establishing polarized light field microscopy as a versatile, simultaneous combination of orthoscopic and conoscopic imaging. This was possible, because the sample was a thin film and imaging rays passed only once through a single crystalline region. For thicker, more complex samples, it proved difficult to ascertain algorithms that can reconstruct thick objects whose birefringence and optic axis orientation varies in 3D, which is typical for most biological and fabricated materials. While difficult, it seems not impossible, especially when we allow for some approximations and simplifying assumptions, and take advantage of the rise of deep learning, including its role in finding solutions to inverse problems in imaging [8].

While with the current paper we do not present a solution to the inverse problem in polarized light imaging, we present a forward solution that accurately predicts polarized light field images of simple objects based on a ray tracing model. We recorded experimental point spread functions using the light field LC-PolScope to image small (∼1 µm diameter) calcite crystals and compare the results to simulated point spread functions based on polarized light ray tracing that implements the Jones calculus for rays that traverse a rasterized object space. By establishing a forward model for polarized light field imaging, we are presenting a critical piece to solving the puzzle of finding solutions to the ill-posed, nonlinear inverse problem in polarized light microscopy.

Following next is the Methods section, where we briefly review the experimental setup, which was described before [7,9]. We also present the newly developed polarized light ray tracing method for light field imaging, implemented and available online as a Mathematica Notebook (Mathematica by Wolfram Research, Chicago, IL) as we show in Code 1, Ref. [10]. In addition to the executable code, the notebook features extensive text and graphics entries with additional explanations and clarifications that can be examined using the Wolfram Player, which is freely available from the Wolfram Research website. In the Results section, we present experimentally recorded and simulated light field images of both, small calcite crystals and of larger dome-like calcite structures and compare their similarities and differences. In the Discussion section, we address questions about our assumptions, including the neglect of diffraction effects and the assumption of straight ray paths through object space, to make the simulation code tractable.

2. METHODS

A. Light Field LC-PolScope

The principles of the LC-PolScope were described elsewhere [11]. The optical setup used for the current study was assembled around a Nikon Eclipse Ti inverted stand, enhanced by a universal, liquid-crystal-based polarizer from Meadowlark Optics Inc. (Frederick, CO, USA), and a light field camera. Figure 1 shows a schematic of the setup assembled on an upright stand. The light field camera is composed of a microlens array and a conventional 2D CCD or CMOS sensor. The specs of the sensor and microlens array were adapted to the magnification and numerical aperture (NA) of the microscope optics. We used a microlens array (RPC Photonics, Rochester, NY) with a pitch of 100 µm and a focal length of 2.5 mm. A 1:1 relay lens made of two AF Nikkor objective lenses ($f = 50$ mm, $f/1.4$, mounted nose to nose, from Nikon, Melville, NY) projected the microlens focal plane onto a CMOS camera (Hamamatsu Photonics Flash4 C13440). The sample was illuminated with a direct current-stabilized 100 W tungsten halogen lamp through a band-pass interference filter (544/24 nm, Semrock Inc, Rochester, NY), a variable LC-polarizer, and an oil immersion condenser lens whose aperture diaphragm was set to 1.2 NA. The sample illuminated by transmitted light was imaged with a Nikon 60×/1.4 NA PlanApo oil immersion objective. The objective lens was followed by a fixed polarization analyzer for left circularly polarized light.

The variable LC polarizer (also called universal compensator) is an optically bonded assembly of two liquid crystal variable retarders and a linear polarizer, which was placed in the illumination path of the microscope. Several predetermined polarization settings can be registered in the controller of the universal polarizer and are used to sequentially acquire five raw images with the light field camera. We call the five raw images together with two computed images of retardance and orientation values a PolStack. For image acquisition and analysis, we used plug-ins designed for Micro-Manager (Micro-Manager.org) and available on the OpenPolScope.org website.

The standard processing algorithms for images recorded with an LC-PolScope setup generate maps of retardance and slow axis orientation values measured for every pixel of a light field image. Both the retardance and slow axis orientation of a given pixel and its associated ray represent the polarization optical properties encountered during the passage of the ray through the optical setup, including the specimen and the lenses and other optical components located between the universal polarizer and the circular analyzer. Fortunately, LC-PolScope algorithms include the ability to remove the contributions of polarization distortions induced by stress in glass or other optical effects in microscope components other than the specimen itself [11,12]. This background correction is based on acquiring a so-called Background PolStack that represents the instrument only and is typically recorded by imaging a clear area within the microscope slide and coverslip assembly that also holds the specimen structures of interest.

The ability to remove the effect of polarization aberrations induced by the instrument will be important in setting up the polarized light ray tracing method described next.
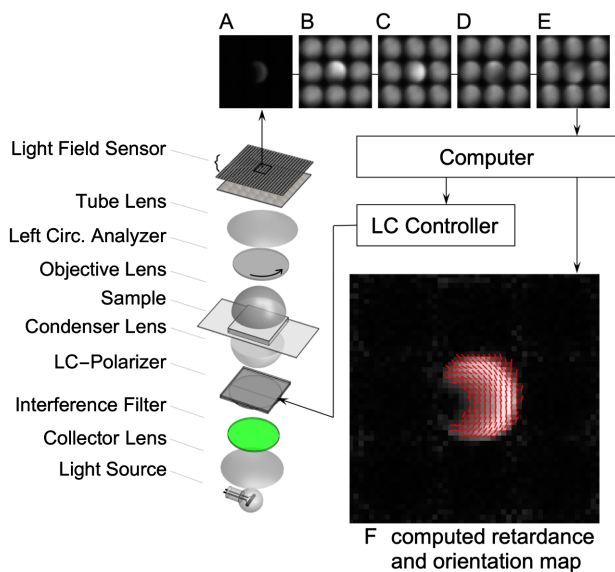
Fig. 1. Schematic of the light field LC-PolScope. The top row of panels **A** through **E** show the raw light field LC-PolScope images of a small calcite crystal that is in focus and centered on a 3-by-3 array of microlenses [same crystal as in Figs. 2(A) and 2(B)]. Panel (F) in the lower right corner shows the measured retardance as a grayscale map and slow axis orientations indicated by short red lines for every pixel. The images in panels (A) through (E) show the acquired intensity behind each microlens, where each panel was recorded using a different setting of the variable LC-Polarizer. Panel (A) was recorded with the LC-Polarizer set for right circularly polarized light, which is blocked by the left circular analyzer, rendering the image mostly dark, except for the center microlens that projects the light that passed through the crystal. For panels (B) through (E), the LC-Polarizer was set to generate elliptically polarized light with different orientations of the elliptic axes. Elliptically polarized light partially passes the circular analyzer and reveals the circular aperture disk projected behind each microlens. In light field images, we do not show a scale bar, because the dimensions are ambiguous, since image details represent two different conjugate planes in the microscope: the positions of the microlenses represent distances in object space, which is sampled on a 1.7 μm square grid, while the 16 by 16 pixels within a square represent the objective's back focal plane, which represents angular coordinates of the rays that path through object space.

B. Polarized Light Ray Tracing

Light field imaging lends itself to be modeled by ray tracing, as the four-dimensional light field image identifies a large but finite set of individual rays that pass through a specific location and direction in object space, as outlined in Marc Levoy's original article [6]. Obviously, this approach neglects diffraction, and it also seems to suffer from a variation in resolution depending on the distance of the reconstructed region from the nominal focus plane in object space [13]. Nevertheless, our success demonstrated in this paper of recording and simulating polarized light field images of birefringent objects between 1 and 100 μm diameter supports our goal of establishing a first forward model for this complex imaging mode.

In addition to limiting ourselves to ray optics, we also make the following assumptions and simplifications: (1) the heterogeneous object material is transparent and only exhibits birefringence as optical anisotropy; (2) variations of the average

refractive index in the object are small; and (3) the object of interest is embedded in a medium that nearly matches its average refractive index. Taken together, these assumptions and simplifications justify the approximation that polarized light rays traverse object space in straight lines and maintain their overall intensity and degree of polarization while changing their polarization state due to the birefringent voxels in simulated objects. The latter assumption that the degree of polarization does not change by the interaction of light with the object allows us to use the Jones calculus for simulating the changes in polarization as the light passes through the object.

The simulation code is available as a Mathematica Notebook and is an open-source companion piece to this article (Code 1, Ref. [10]). The Notebook is extensively annotated, including text and graphics entries that describe the simulation framework and the mapping between camera pixels and their associated light rays. A ray is uniquely identified by its propagation direction $\overline{rayDir}$ and a location (x, y, z) in object space. Here we briefly summarize the mathematical expressions used to calculate the retardance and azimuth accumulated by a given ray as it passes through the birefringent object.

Objects are described by a rasterized volume whose cubic voxels (side length typically ~0.5 μm) can each possess a uniaxial birefringence Δn, which can be positive, negative, or zero. The description of the birefringence of a voxel also includes the optic axis direction given by a unit vector $\overrightarrow{oa}$ in object space coordinates. Individual voxels are identified by indices (i, j, k) that describe the voxel's position along the three coordinate axes that span object space. For identifying the voxels that a ray with a given position and direction will intersect on its path through object space, we took the algorithms first proposed by Siddon [14] and implemented them in Mathematica code. For a given ray, the algorithms identify the (i, j, k) indices of the voxels that are sequentially traversed by the ray and the ray's intersection lengths for each voxel. We represent the linear list of voxel indices (i, j, k) and intersection lengths l by a single index v that identifies the birefringence value Δn_v, optic axis direction $\overrightarrow{oa}_v$, and intersection length l_v for each voxel v traversed in sequence by the light ray.

With those definitions, we are almost ready to write the expressions for the retardance and azimuth of the slow axis, accumulated over the ray's path through object space. However, to compute a retardance Jones matrix, we still need to define two directions that span the plane perpendicular to the propagation direction of the ray. Every Jones matrix associated with a ray is defined in the plane perpendicular to the ray direction. To use a coordinate system that is common to all rays, regardless of their propagation direction in object space, we choose the laboratory frame of reference where all rays propagate parallel to the x axis after they have been reoriented by the microscope objective lens. This reorientation is described by a rotation matrix that takes a vector along the ray direction in object space and rotates it parallel to the x axis. We then apply the inverse of this rotation matrix to unit vectors that are parallel to the y and z axis to define the vectors that span the plane perpendicular to the ray direction and call the rotated vectors $\overline{ray_y}$ and $\overline{ray_z}$. With this notation, $\overline{rayDir}$ is equivalent to $\overline{ray_x}$. This will also allow us to compare our simulation results to our experimental measurements, which are taken using polarization components,

such as polarizers and retarders, whose optical axes are aligned with the laboratory frame of reference.

To calculate the retardance ret_v that is associated l_v with a single birefringent voxel v and a ray with direction $\overrightarrow{rayDir}$, we take the square of the scalar product between the voxel's optic axis $\overrightarrow{oa}_v$ and $\overrightarrow{rayDir}$, and multiply the result with the voxel's birefringence Δn_v and with the ray's intersection length l_v [7,15]:

$$ret_v = \Delta n_v \left(1 - \left| \overrightarrow{oa}_v \cdot \overrightarrow{rayDir} \right|^2 \right) l_v \frac{2\pi}{\lambda}. \quad \textbf{(1)}$$

The expression $(1 - |\overrightarrow{oa}_v \cdot \overrightarrow{rayDir}|^2)$ is equal to $\sin^2\alpha$, where α is the angle between the ray direction and the optic axis, and the factor $2\pi/\lambda$ converts the retardance from a length (typically in nanometers) to radians, where λ is the wavelength of the light.

The slow axis orientation or azimuth $azim_v$ that is associated with retardance ret_v refers to an angle in the plane spanned by $\overrightarrow{ray}_y$ and $\overrightarrow{ray}_z$ and is measured from the $\overrightarrow{ray}_y$ axis. $azim_v$ is given by the scalar products between the optic axis $\overrightarrow{oa}_v$ and unit vectors $\overrightarrow{ray}_y$ and $\overrightarrow{ray}_z$:

$$azim_v = \tan^{-1} \left(\frac{\overrightarrow{oa}_v \cdot \overrightarrow{ray}_y}{\overrightarrow{oa}_v \cdot \overrightarrow{ray}_z} \right). \quad \textbf{(2)}$$

With expressions for $azim_v$ and ret_v, we are now ready to define the retardance Jones matrix $\overline{retJM}_v$, associated with voxel v and ray direction $rayDir$ [16]:

$$\overline{retJM}_v = \begin{bmatrix} \cos\left(\frac{ret_v}{2}\right) - i\cos(2azim_v)\sin\left(\frac{ret_v}{2}\right) & -i\sin(2azim_v)\sin\left(\frac{ret_v}{2}\right) \\ -i\sin(2azim_v)\sin\left(\frac{ret_v}{2}\right) & \cos\left(\frac{ret_v}{2}\right) + i\cos(2azim_v)\sin\left(\frac{ret_v}{2}\right) \end{bmatrix}. \quad \textbf{(3)}$$

For the simulations presented here, a ray sequentially passes through typically 10 to 100 voxels, some of which will not be birefringent ($\Delta n_v = 0$), and others will carry some birefringence. To generate the Jones matrix $\overline{rayJM}$ of the accumulated retardance and final azimuth value for a given ray, we form the product of the individual Jones matrices of the voxels that are traversed in a linear sequence given by the index v that increases from 1 to N:

$$\overline{rayJM} = \prod_{v=1}^{N} \overline{retJM}_v. \quad \textbf{(4)}$$

N is the total number of voxels traversed and, as stated earlier, can vary between 10 and 100, depending on the size of the object and the ray direction. As is well known for the Jones calculus, the order in which the ray traverses the individual birefringent voxels is important because the Jones matrices generally do not commute in a product of matrices.

The text and graphics in the Mathematica Notebook give further details about the simulation code and the generation of a simulated light field image that is composed of a rectangular array of small aperture images. Individual aperture images are composed of 172 pixels, arranged in disk shape, and each pixel value is the result of applying expressions for either recovering the retardance or the azimuth value from $\overline{rayJM}$ that is associated with that pixel. An illustration of the circular aperture disk of

retardance values and slow axis orientations generated behind a single microlens is seen in the middle panel ($z = 0$) of Fig. 3(B).

As already alluded to, the experimental maps of specimen retardance and slow axis orientation are background corrected and represent data associated with the specimen only. Hence, for generating ray tracing results that can be compared to the experimental data, we only consider the ray paths that extend between an entrance and exit plane, between which the simulated object is located in object space and that are typically less than 100 μm apart.

3. RESULTS

A. Experimental and Simulated Point Spread Functions

Calcite is a uniaxial, negatively birefringent crystal of calcium carbonate ($CaCO_3$). Small single crystals (diameters down to 1 μm and smaller) were prepared as precipitate by mixing, in approximately stoichiometric amounts, saturated aqueous solutions of sodium bicarbonate and calcium chloride (see [3]). A small amount of solution with precipitate was transferred to a microscope cover glass. Unreacted amounts of the original compounds were rinsed away with purified water. Crystals that adhered to the cover glass were allowed to dry and were embedded in Permount, which is a clear resin that has a refractive index of 1.52, matching the refractive index of the cover glass and microscope slide (all reagents and supply items from Fisher Scientific).

We recorded experimental point spread functions using the LC-PolScope equipped with a 60×/1.4 NA apochromat oil immersion objective lens and an oil immersion condenser lens, whose numerical aperture was stopped down to 1.2. Figure 2 shows two experimental and one simulated set of retardance images representing three focus series of the same 1-μm-sized calcite crystal. Images in the top row [Fig. 2(A)] were recorded using a regular camera (no microlens array) whose sensor was placed directly in the image plane of the microscope. The in-focus image at $z = 0$ barely resolves the diamond shape of the crystal that seems to have one of the typical calcite cleavage forms, a rhombohedron. The optic axis direction bisects the obtuse angle of the diamond shape and is tilted by 45° to the microscope axis (see, e.g., [3]). The tilt in the optic axis direction is apparent in the second focus series [Fig. 2(B)], which was recorded with the light field camera. When the crystal is at $z = 0$, all the light that has passed through the crystal is collected by a single microlens that projects the conoscopic image onto the camera sensor. The edge of the conoscopic image corresponds to a numerical aperture of 1.2, which, in object space, is associated with a tilt angle of 52° to the microscope axis. Hence, rays that are parallel to the optic axis of the crystal are still within the recorded aperture and can be recognized by the near zero
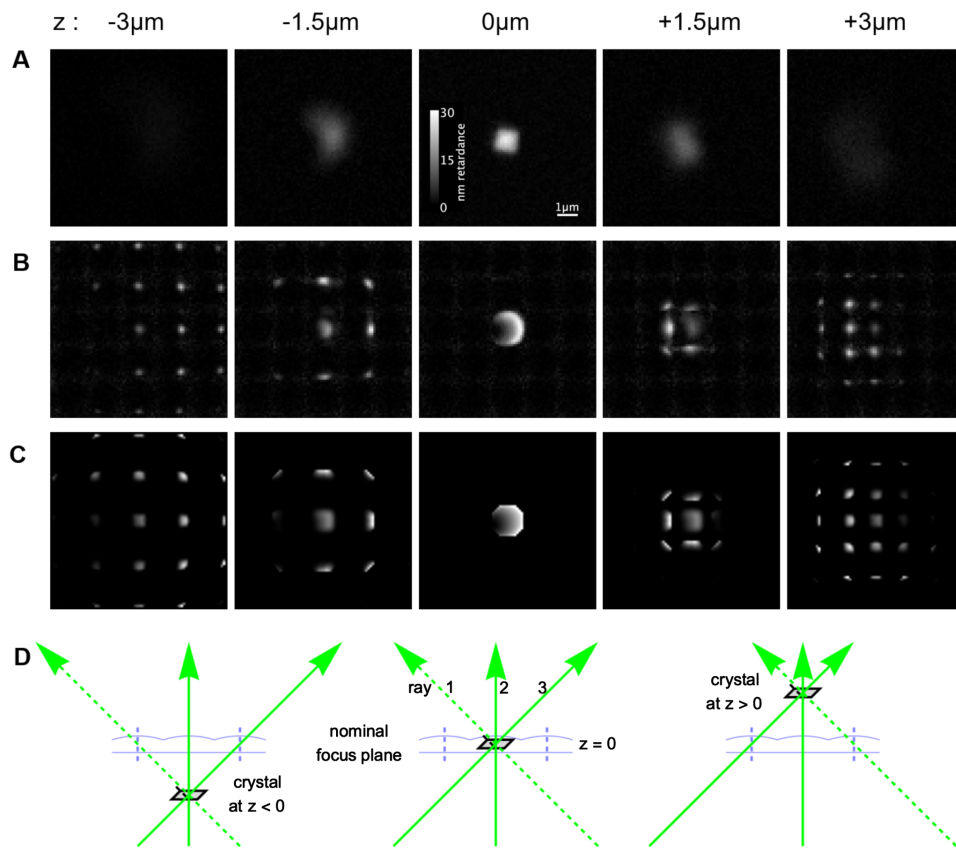
Fig. 2. Focus series ($-3\,\mu m \leq z \leq +3\,\mu m$, $z = 0$ in-focus object plane) of retardance images of a small calcite crystal embedded in immersion oil ($n = 1.52$) and recorded with the LC-PolScope equipped with a $60\times/1.4$ NA oil immersion objective and matching condenser optics, whose aperture was reduced to 1.2 NA. Row (A) shows the crystal in a focus series using a regular camera in the microscope's image plane. Row (B) shows the same crystal with the microlens array in the image plane and the camera in the focal plane of the microlenses (light field camera). Row (C) shows simulated retardance images of a birefringent ball object of similar size (diameter 1 μm), birefringence (-0.172), optic axis orientation (45° tilt to microscope axis), and focus positions as the experimental crystal. The retardance calibration bar and 1 μm scale bar in row (A) and $z = 0$ apply to all retardance images. Row (D) is a series of schematics showing the crystal positions in object space along the microscope axis (z axis) relative to the microlens array, shown in blue as projected into object space by the microscope objective lens. As explained in the caption to Fig. 1, we do not show scale bars in light field images.

retardance recorded in the black spot near the 9 o'clock position in the central aperture of the light field image at $z = 0$. The schematic in Fig. 2(D) illustrates this relationship. For z positions other than 0, tilted rays are collected by lenses other than the one centered on the crystal. The schematic also illustrates the geometric relationship between light field patterns for crystal positions below ($z < 0$) and above ($z > 0$) the nominal focus plane.

For $z < 0$, tilted rays that interacted with the crystal are collected near the aperture edge that is farthest from the central microlens, while for $z > 0$, the tilted rays are collected near the edge that is closest to the central microlens.

We also note the stark difference in retardance levels measured in out-of-focus images when using the conventional camera [Fig. 2(A)] versus the light field camera [Fig. 2(B)]. In conventional images, the crystal retardance measured for $z = 3\,\mu m$, for example, becomes spread over many pixels, each registering only a small retardance value that becomes too small to be measured and is drowned by image noise. In the light field image, however, the retardance carried by rays is only shared between a few pixels, even for out-of-focus crystal positions,

and retardance values remain measurable even for quite far out-of-focus positions.

All these features in the experimental images are well reproduced in the simulated light field images shown in Fig. 2(C), which were computed using specifications and parameters that closely match the experimental ones (for further details, please see text entries in the companion Mathematica Notebook.)

In Fig. 3(A), retardance light field images of another small calcite crystal are shown, whose optic axis orientation is nearly parallel to the microscope axis. The crystal was found in the same preparation as the one in Fig. 2 and likely had a columnar shape, another common crystal habit of calcite. The light field panels include red lines indicating the slow axis orientations measured together with the retardance of each pixel. For the in-focus image ($z = 0$), the lines are oriented tangentially around the central dark region, because calcite is negatively birefringent, orienting the high refractive index axis perpendicular to the optic axis projection for each ray. Again, the complementarity of the retardance patterns for crystal positions below and above the nominal focus plane can be readily observed. This complementarity also extends to the patterns of orientation lines observed
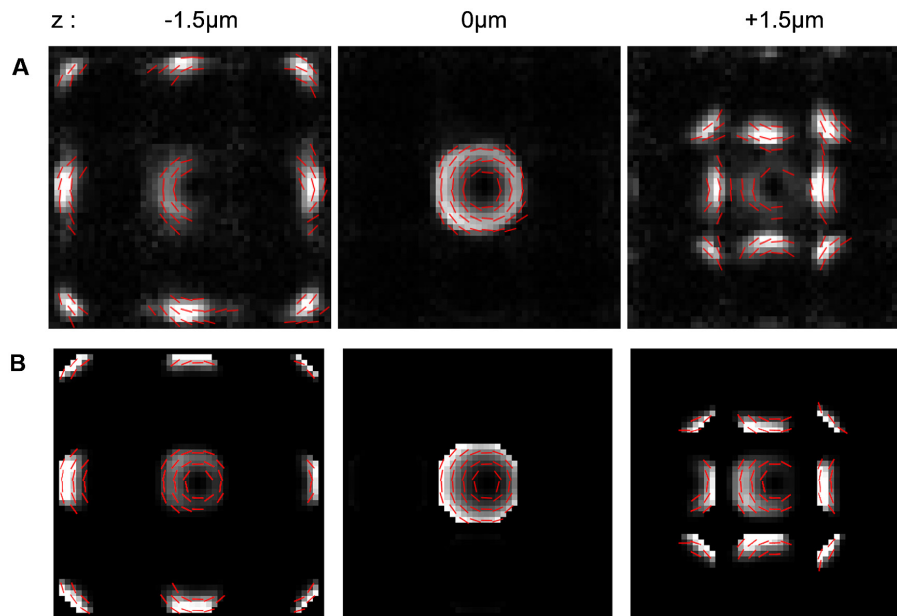
Fig. 3. Focus series of light field retardance images of a small columnar calcite crystal in which the crystal's optic axis is nearly parallel to the microscope axis. Red lines indicate the slow axis orientation for every other pixel. Row (A) shows experimental images of a columnar crystal that we found in the same preparation as the rhombohedron crystal in Fig. 2. Row (B) shows simulated retardance images of a birefringent cylinder of similar size (diameter 1 μm, length 1.2 μm). In both rows, the out-of-focus images are contrast enhanced by a factor of 2 for better visibility of the orientation lines.

behind microlenses surrounding the central microlens. For both positions ($z < 0$ and $z > 0$), though, the slow axis orientations remain tangential to the center of the projected aperture disk behind a given microlens.

All these features observed in the experimental images of row (A) are well reproduced in the simulated images of row (B) in Fig. 3. While further details of the simulation conditions are described in the companion Mathematica Notebook, we stress that the detailed light field patterns of the simulation depend only on a few adjustable parameters for the sample object, such as the size and position of the simulated crystal, the two orientation angles specifying the solid angle of its optic axis, and its birefringence. Because of the small size of the crystal (diameter ∼1 μm) relative to the projected microlenses (diameter 1.73 μm), the simulation is insensitive to the exact shape of the crystal.

B. Light Field Images of a Juvenile Clamshell

For objects larger than 1 μm, size and shape matter. To further explore the validity of our ray tracing method, we compare experimental results and simulations for a larger birefringent object. Recently, we published polarized light field images of juvenile clamshells, which represent simple dome-shaped objects that are moderately birefringent and whose optic axis orientations vary systematically across the shell surface [9]. We have reexamined a set of images from that study and set up a simulation of a dome-like object of similar size and shape.

Figure 4 summarizes the experimental and ray tracing results as light field images of a 100-μm-wide juvenile clam shell and its simulation as a calcite dome. The structures are embedded in

a medium (oil) whose refractive index of 1.52 closely matches their average refractive index.

After examining the light field images of the experimental clamshell [Fig. 4(A)] and the corresponding simulated images [Fig. 4(B)], it is apparent that the simulated dome is not fully representative of the clamshell, which has irregularities, and one side is flattened where the hinge of the bivalve will develop. Nevertheless, the prominent features of the experimental light field images are reproduced by the simulation.

Top regions of the shell and dome, both show aperture retardance images that are typical for a negatively birefringent sheet, whose optic axis is parallel to the microscope axis. As we move closer to the outer edge of the shell/dome, the optic axis becomes more inclined, and the dark spot in the aperture image moves away from the aperture center in a systematic fashion that is well reproduced in the simulated images.

The magnitude of retardance in an aperture image near the top of the shell is reproduced in the simulation by assuming a thickness of ∼0.5 μm for the calcite dome. As the microlens position moves closer to the edge of the shell, the dark spot moves away from the center, and higher retardance values appear on the side opposite the dark spot. The measured increase, however, cannot be explained by a rotation of the optic axis alone. The simulated aperture images near the edge of the dome become more like the experimental ones if we account for an increase in the thickness of the dome and by extension of the shell.

The two enlarged microlens arrays on the left side in Fig. 4(B) illustrate another finding that is related to the above point. Both the experimental and simulated aperture images near the edge show a sudden decrease of the measured retardance where we would have expected a continued increase in retardance.
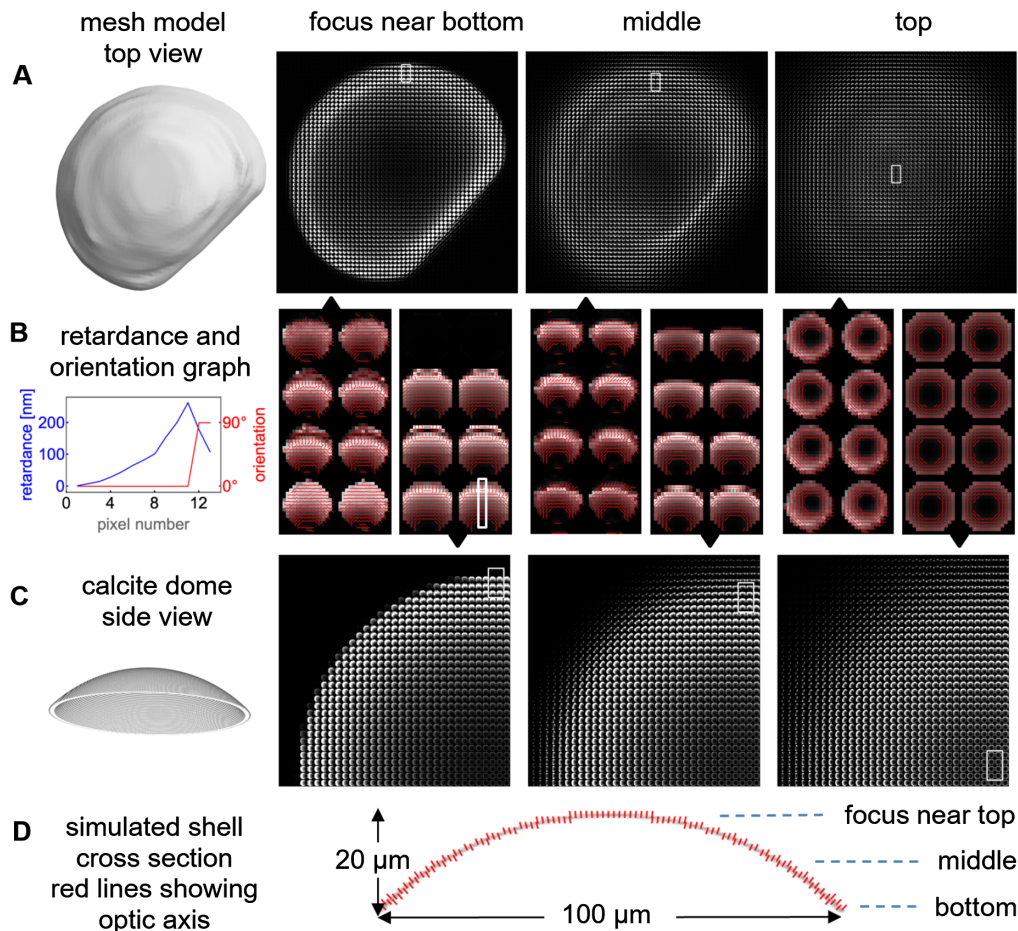
Fig. 4. Light field retardance images of a juvenile clamshell [row (A)] and of a simulated calcite dome [row (C)] that were recorded/simulated with the object in three different focus positions (images in (C) only show the top left quarter of the full light field image of the simulated calcite dome). Row (B) shows enlarged arrays of 2-by-4 microlenses, picked from corresponding regions of the experimental and simulated images, as indicated by white frames in images of rows (A) and (C). The red lines in (B) show the slow axis orientations for points in the aperture images of each microlens. The graph on the left side of (B) plots the retardance and slow axis orientation along a vertical aperture strip, indicated by the white frame in the second image from the left. The graph shows an inflection of the retardance and a jump by 90° in the orientation, which is a measurement artifact that is expected if retardance values increase beyond half a wavelength (see text). Row (D) shows a cross section of the simulated dome whose thickness slightly increases from ∼0.5 µm at the top to ∼1 µm near the bottom. The voxel size for the simulation is 0.57 µm. The field of view in (A) is about 100 µm square, while in (B) it is about 50 µm square, both in object space dimensions.

In addition, in pixels with an unexpected decrease in retardance, the slow axis orientation flips from horizontal (azimuth 0°) to vertical (azimuth 90°). Both these observations are illustrated in the graph of Fig. 4(B). The observation of both phenomena together, sudden drop in retardance near half-wavelength values together with a flip by 90° of the slow axis orientation support the explanation that draws on so-called phase wrapping between the orthogonally polarized rays that interfere to generate the observed polarization. While a full explanation would be too lengthy here, we refer the reader to the website OpenPolScope.org for a more complete description of the phenomenon. Suffice it to say that for the simulation, (a) the Jones calculus, in general, reproduces this experimentally observed phenomenon, and (b) in the specific case of the clamshell, the measured retardance near the top region and near the edge can be made compatible only by allowing the shell thickness to increase from the top to the edge of the shell/dome by a factor of about 2.

4. DISCUSSION

We found that the simulated light field images of a small, birefringent sphere are remarkably close to the experimental retardance images of a small calcite crystal (crystal diameter < microlens diameter). All the distinct features of the retardance light field images are reproduced, including the distribution of retardance and the associated slow axis orientation among several microlenses as the crystal/sphere is moved in and out of focus. And yet, there are also distinct differences between the experimental and simulated light field images that are due in part to the assumptions and simplifications we have introduced when establishing the ray tracing model.

Among the more impactful simplifications is the neglect of diffraction that occurs on stops and apertures of the imaging optics, including the diffraction on the aperture stop of the microscope objective lens. The diffraction on the aperture stop leads to the broadening of the image of a point source to the

well-known Airy pattern, whose central maximum is broadened to $1.22 \frac{\lambda}{NA}$ in object space units, with NA the numerical aperture of the objective lens. In our experiments and simulations, the central Airy disk that is projected onto the microlens array when the point source is in the nominal focus plane, has a diameter of $60 \times 1.22 \frac{\lambda}{NA} = 15$ μm compared to the 100 μm square microlens diameter. The size of the calcite crystal image and its simulated counterpart is 60 μm, and broadening by diffraction is expected to be a minor effect. Another possible contribution might come from the diffraction on the square aperture of the microlenses and is detected on the light sensor, which is in the focal plane of the lenslets. Together, we expect the diffraction effects to account for the additional blur of measured retardance values observed in the experimental versus simulated images. To properly account for all the diffraction effects, it will be necessary to expand the simulation presented here with approaches that include wave optical effects. For fluorescence light field microscopy, this was done by Broxton *et al*. and by Quicke *et al*., with the latter expanding the first treatment to allow for dipole emitters and high NA objective lenses [13,17].

Another approximation we have used is the assumption that light rays traverse object space in straight lines. This is based on two observations: (1) the refractive index in object space varies by less than 10% between object and surrounding medium, and (2) the objects themselves are small and/or thin, so that the interaction length of rays with the object is of the order of a few micrometers. These observations seem to be related to the applicability of the Born or Rytov approximation in diffraction tomography, for example [18]. In a recent paper, Yeh *et al.* described the use of the Born approximation in developing solutions to the inverse problem in polarized light imaging with oblique illumination [19]. In conjunction with ray tracing, it is interesting to note that the Born approximation cannot reproduce refraction of a beam of light traversing a dielectric interface [20]. Hence, it seems that the assumption of a straight ray path through object space has a similar range of validity as the Born approximation. Therefore, our assumption of straight ray paths seem well justified for most materials and biological cells and tissues whose interaction with light can be described with sufficient accuracy by the Born approximation.

We developed the ray tracing model for generating polarized light field images of simulated objects with two purposes in mind: (1) the program is used to generate light field images of objects that are configured as close as possible to real objects that were observed in our experiments; (2) the program can also be used to compute polarized light field images of any conceivable object shape and configuration for generating a multitude of simulated pairs of light field images and their ground truth 3D objects. Such pairs can then be used to train suitably configured computational neural networks that can generate 3D object models that closely resemble their ground truths but whose pairs were not part of the training set. When we say, "suitably configured computational neural networks," we envision future research into how such networks are optimally configured to provide a fast and efficient solution to the inverse problem of polarized light field microscopy.

To reach our goal of establishing accurate training sets for machine learning and/or analytic approaches to solving the inverse problem in polarized light field imaging, we plan to incorporate diffraction effects into the ray tracing model, and we will explore the use of a three-by-three polarization ray tracing matrix, P, in our model. As a generalized version of the two-by-two Jones matrix, the P-matrix is designed to simplify polarization ray tracing in 3D [21,22]. While we expect computational efficiencies with this approach, we do not expect the results to change between the approach described here and an approach that makes use of the P-matrix.

Finally, we would like to note that the simulation framework presented here can easily be extended to other anisotropies, such as linear and circular dichroism, for which specific Jones matrix representations exist.

5. CONCLUSION

Polarized light field microscopy has the potential to measure, for the first time, the three-dimensional orientations and positions of birefringent structures in biological and fabricated materials in a fast and comprehensive way. Birefringence is a sensitive indicator of structural anisotropy, which can reveal some of the mechanical and dynamic properties of materials and functions in biological cells and tissues. With the current study, we aim to contribute to a computational framework for solving the ill-posed and nonlinear inverse problem in polarized light field microscopy and, more generally, multiview polarized light imaging.

To this end, we presented experimental point spread functions of the Light Field LC-PolScope and compared them to simulated point spread functions based on a ray tracing model. The method itself and further explanations, including results, are published in a Mathematica Notebook that is an open-source companion piece to this paper.

Disclosures. The authors declare that there are no conflicts of interest related to this paper.

Data availability. Data underlying the results presented in this paper are not publicly available at this time but may be obtained from the authors upon reasonable request.

REFERENCES

1. B. Richards and E. Wolf, "Electromagnetic diffraction in optical systems. II. Structure of the image field in an aplanatic system," Proc. R. Soc. London A **253**, 358–379 (1959).
2. S. F. Gibson and F. Lanni, "Experimental test of an analytical model of aberration in an oil-immersion objective lens used in three-dimensional light microscopy," J. Opt. Soc. Am. A **9**, 154–166 (1992).
3. R. Oldenbourg and P. Török, "Point-spread functions of a polarizing microscope equipped with high-numerical-aperture lenses," Appl. Opt. **39**, 6325–6331 (2000).

4. M. Shribak and R. Oldenbourg, "Mapping polymer birefringence in three dimensions using a polarizing microscope with oblique illumination," Proc. SPIE **5462**, 57–67 (2004).

5. S. M. Guo, L. H. Yeh, J. Folkesson, I. E. Ivanov, A. P. Krishnan, M. G. Keefe, E. Hashemi, D. Shin, B. B. Chhun, N. H. Cho, M. D. Leonetti, M. H. Han, T. J. Nowakowski, and S. B. Mehta, "Revealing architectural order with quantitative label-free imaging and deep learning," Elife **9**, e55502 (2020).

6. M. Levoy, R. Ng, A. Adams, M. Footer, and M. Horowitz, "Light field microscopy," ACM Trans. Graph. **25**, 924–934 (2006).

7. R. Oldenbourg, "Polarized light field microscopy: an analytical method using a microlens array to simultaneously capture both conoscopic and orthoscopic views of birefringent objects," J. Microsc. **231**, 419–432 (2008).

8. K. de Haan, Y. Rivenson, Y. Wu, and A. Ozcan, "Deep-learning-based image reconstruction and enhancement in optical microscopy," Proc. IEEE **108**, 30–50 (2020).

9. M. T. Tran and R. Oldenbourg, "Mapping birefringence in three dimensions using polarized light field microscopy: the case of the juvenile clamshell," J. Microsc. **271**, 315–324 (2018).

10. R. Oldenbourg, "Mathematica code: polarized light ray tracing for light field imaging with the microscope," figshare, 2022, https://doi.org/10.6084/m9.figshare.19695319.

11. R. Oldenbourg and G. Mei, "New polarized light microscope with precision universal compensator," J. Microsc. **180**, 140–147 (1995).

12. M. Shribak and R. Oldenbourg, "Techniques for fast and sensitive measurements of two-dimensional birefringence distributions," Appl. Opt. **42**, 3009–3017 (2003).

13. M. Broxton, L. Grosenick, S. Yang, N. Cohen, A. Andalman, K. Deisseroth, and M. Levoy, "Wave optics theory and 3-D deconvolution for the light field microscope," Opt. Express **21**, 25418–25439 (2013).

14. R. L. Siddon, "Fast calculation of the exact radiological path for a three-dimensional CT array," Med. Phys. **12**, 252–255 (1985).

15. M. Born and E. Wolf, *Principles of Optics: Electromagnetic Theory of Propagation, Interference and Diffraction of Light*, 7th ed. (Cambridge University, 2002).

16. C. Brosseau, *Fundamentals of Polarized Light: A Statistical Optics Approach* (Wiley, 1998).

17. P. Quicke, C. L. Howe, P. Song, H. V. Jadan, P. L. Dragotti, T. Knopfel, A. J. Foust, S. R. Schultz, and M. Neil, "Calculation of high numerical aperture lightfield microscope point spread functions," in *Imaging and Applied Optics 2019 (COSI, IS, MATH, pcAOP), OSA Technical Digest* (Optical Society of America, 2019), paper CW4A.2.

18. B. Chen and J. J. Stamnes, "Validity of diffraction tomography based on the first Born and the first Rytov approximations," Appl. Opt. **37**, 2996–3006 (1998).

19. L.-H. Yeh, I. E. Ivanov, J. R. Byrum, B. B. Chhun, S.-M. Guo, C. Foltz, E. Hashemi, J. A. Pérez-Bermejo, H. Wang, Y. Yu, P. G. Kazansky, B. R. Conklin, M. H. Han, and S. B. Mehta, "uPTI: uniaxial permittivity tensor imaging of intrinsic density and anisotropy," bioRxiv:2020.12.15.422951 (2021).

20. M. L. Oristaglio, "Accuracy of the Born and Rytov approximations for reflection and refraction at a plane interface," J. Opt. Soc. Am. A **2**, 1987–1993 (1985).

21. G. Yun, K. Crabtree, and R. A. Chipman, "Three-dimensional polarization ray-tracing calculus I: definition and diattenuation," Appl. Opt. **50**, 2855–2865 (2011).

22. G. Yun, S. C. McClain, and R. A. Chipman, "Three-dimensional polarization ray-tracing calculus II: retardance," Appl. Opt. **50**, 2866–2874 (2011).